JCB Journal of Cell Biology

REPORT

Recognition of RNA by the S9.6 antibody creates pervasive artifacts when imaging RNA:DNA hybrids

John A. Smolka, Lionel A. Sanz, Stella R. Hartono, and Frédéric Chédin

The S9.6 antibody is broadly used to detect RNA:DNA hybrids but has significant affinity for double-stranded RNA. The impact of this off-target RNA binding activity has not been thoroughly investigated, especially in the context of immunofluorescence microscopy. We report that S9.6 immunofluorescence signal observed in fixed human cells arises predominantly from ribosomal RNA, not RNA:DNA hybrids. S9.6 staining was unchanged by pretreatment with the RNA:DNA hybrid–specific nuclease RNase H1, despite verification in situ that S9.6 recognized RNA:DNA hybrids and that RNase H1 was active. S9.6 staining was, however, significantly sensitive to RNase T1, which specifically degrades RNA. Additional imaging and biochemical data indicate that the prominent cytoplasmic and nucleolar S9.6 signal primarily derives from ribosomal RNA. Importantly, genome-wide maps obtained by DNA sequencing after S9.6-mediated DNA:RNA immunoprecipitation (DRIP) are RNase H1 sensitive and RNase T1 insensitive. Altogether, these data demonstrate that imaging using S9.6 is subject to pervasive artifacts without pretreatments and controls that mitigate its promiscuous recognition of cellular RNAs.

Introduction

RNA:DNA hybrids have emerged as a biologically interesting and potentially disease-relevant species of nucleic acid. In particular, R-loops, RNA:DNA hybrids that form via hybridization of single-stranded RNA (ssRNA) to a complementary strand of a DNA duplex, displacing the other DNA strand into a single-stranded state, have been proposed to cause DNA damage and regulate various cellular processes (Aguilera and García-Muse, 2012; Chédin, 2016; Crossley et al., 2019). R-loop formation is thought to be a primarily cotranscriptional phenomenon (Sanz et al., 2016), and elevated R-loop levels have been invoked by many studies as a link between transcription and genomic instability (Hatchi et al., 2015; Huertas and Aguilera, 2003; Li and Manley, 2005; Nguyen et al., 2017; Paulsen et al., 2009; Stirling et al., 2012). Much of the supporting evidence has relied on the use of the S9.6 mouse monoclonal antibody. S9.6 was initially reported to specifically recognize RNA:DNA hybrids (Boguslawski et al., 1986) and has thus been widely used to isolate, sequence, measure, and image RNA:DNA hybrids in a variety of cell types from a variety of organisms (Bayona-Feliu et al., 2017; El Hage et al., 2014; Ginno et al., 2012; Skourti-Stathaki et al., 2011; Sorrells et al., 2018; Xu et al., 2017; Zeller et al., 2016).

Since the initial report on S9.6 from Boguslawski et al. (1986), subsequent studies have shown that S9.6 can also bind double-stranded RNA (dsRNA; Hartono et al., 2018; Kinney et al., 1989) with an affinity similar to its affinity for RNA:DNA hybrids (Phillips et al., 2013). This has made the use of RNase H enzymes, nucleases that specifically degrade the RNA strand of RNA:DNA hybrids, critical in verifying the RNA:DNA hybrid dependence of measurements made using S9.6-based assays (Vanoosthuyse, 2018). While RNase H pretreatments are routinely used as negative controls in molecular S9.6-based methods like immunoprecipitations and dot blots, cellular imaging using S9.6 is often reported without exogenous RNase H treatment (Choi et al., 2018; Kabeche et al., 2018; Nguyen et al., 2018; Nguyen et al., 2017; Shen et al., 2017; Skourti-Stathaki et al., 2014; Wang et al., 2018). When RNase H controls are implemented, results vary from study to study, with some studies reporting removal of S9.6 immunofluorescence (IF) signal by exogenous RNase H treatment and others finding RNase H–resistant signal (Barroso et al., 2019; Hamperl et al., 2017; Silva et al., 2018; Sollier et al., 2014; Wahba et al., 2013). Additionally, the S9.6 staining pattern itself varies from study to study, often coincident with methodological differences in fixation, permeabilization, and buffers used to prepare and/or enzymatically treat cells before immunolabeling (De Magis et al., 2019; Hamperl et al., 2017; Marinello et al., 2013; Nguyen et al., 2017; Silva et al., 2018; Skourti-Stathaki et al., 2014; Sollier et al., 2014). Lastly, although a common goal of using S9.6 is to image R-loop structures in the nucleus, prominent cytoplasmic S9.6 signal has been consistently observed across studies. This signal is often unaddressed

Department of Molecular and Cellular Biology and Genome Center, University of California, Davis, Davis, CA.

Correspondence to Frédéric Chédin: flchedin@ucdavis.edu.

or attributed to R-loops arising from the mitochondrial genome (Ginno et al., 2012) or RNA Polymerase III–dependent cytosolic hybrids (Koo et al., 2015). However, conclusive experimental evidence to establish the origin of this signal and its sensitivity to exogenous RNase H treatment is lacking.

In this study, we established a protocol to test the RNA:DNA hybrid and RNA dependence of S9.6 staining using structure-specific nucleases to selectively and separably degrade RNA:DNA hybrids and RNA. In addition, we implemented a positive control for S9.6 staining and in situ RNase H1 activity using synthetic Cy5-labeled RNA:DNA hybrids transfected into human cells before imaging. Using this approach, we verified that exogenous RNA:DNA hybrids can be recognized by S9.6 and degraded by RNase H1 in situ under methanol-fixed conditions. However, we demonstrate that the endogenous structures labeled by S9.6 in normally cultured cells are resistant to pretreatments with RNase H1. In contrast, S9.6 labeling was significantly reduced by pretreatments with enzymes that specifically degrade ssRNA and, to a lesser extent, dsRNA. Lastly, we provide evidence that the off-target RNAs labeled by S9.6 are primarily ribosomal RNAs (rRNAs). Thus, we conclude that images obtained through IF microscopy using the S9.6 antibody are vulnerable to artifactual signal that reflects cellular RNA content, particularly rRNA abundance, not RNA:DNA hybrids.

Results and discussion

RNA constitutes the majority of the S9.6 IF signal in the cytoplasm and nucleus of human cells

Using human U2OS cells fixed with methanol, the most commonly used fixative for S9.6 staining, S9.6 IF signal was observed in both the nucleus and the cytoplasm (Fig. 1 A). Nuclear staining was predominantly nucleolar in morphology and localization. These staining patterns are congruent with multiple previous reports (Choi et al., 2018; Shen et al., 2017; Silva et al., 2018; Skourti-Stathaki and Proudfoot, 2014; Sollier et al., 2014; Sridhara et al., 2017) and have been explained by claims that ribosomal DNA is a hot spot for R-loop formation in the nucleus (El Hage et al., 2010) and that mitochondrial genomes in the cytoplasm contain R-loops (Holt, 2019). To determine if the cytoplasmic S9.6 signal derives from mitochondria, we labeled mitochondria before fixation using the vital dye MitoTracker Deep Red FM and assessed the degree of colocalization with S9.6. Cytoplasmic S9.6 staining had a distribution qualitatively more similar to HSP27, which labels the entire cell body, than to mitochondria (Fig. 1 B), and S9.6 IF signal did not show enrichment in or correlation with mitochondrial territories (Fig. 1 C). These observations agree with prior work in human cells grown under standard conditions (Silva et al., 2018) and indicate that mitochondria are not the source of the majority of cytoplasmic S9.6 staining. Furthermore, these data demonstrate that S9.6 detects an abundance of extramitochondrial structures throughout the cytoplasm.

Informed by previous reports showing that S9.6 can recognize dsRNA in vitro, we hypothesized that various species of cellular RNA in fixed cells may be the source of cytoplasmic S9.6 signal, and possibly nuclear signal as well. To test this hypothesis, we identified ribonucleases that could robustly degrade RNA without degrading RNA:DNA hybrids. Under a magnesium-supplemented condition, which is necessary for RNase H activity (Hyjek et al., 2019), we verified that commercial RNase T1 and RNase III enzymes were capable of specifically and efficiently degrading ssRNA and dsRNA substrates (Fig. S1 A). Importantly, under the same condition, these enzymes had negligible activity on RNA:DNA hybrid substrates (Fig. S1, A and B), and full-length, recombinantly purified human RNase H1 (Loomis et al., 2014) efficiently digested the RNA strand of the RNA:DNA hybrid substrate (Fig. S1 B). However, RNase A degraded RNA:DNA hybrids within 1 h at room temperature (Fig. S1 C), indicating it was not a suitable enzyme to use for specific degradation of RNA. Additionally, ShortCut RNase III degraded RNA:DNA hybrids in the presence of manganese (Fig. S1 D), indicating that the manganese supplementation recommended by New England Biolabs for ShortCut RNase III treatments could not be used.

We tested the effects of validated enzymes in situ on S9.6 staining by subjecting fixed samples to mock or enzymatic treatments before immunolabeling under the same conditions validated by the in vitro tests above. As expected, mock-treated methanol-fixed cells stained with S9.6 showed a primarily pan-cytoplasmic and nucleolar staining pattern (Fig. 2 A). The average nuclear S9.6 intensity was 35.4% of the average total cellular intensity (Fig. 2 B), indicating that cytoplasmic signal was the predominant constituent of the total cellular S9.6 signal. Pretreatment with RNase H1 did not have a significant effect on S9.6 staining in the cytoplasm or the nucleus (Fig. 2, A and B). Pretreatment with RNase III had minimal effect on total cellular signal (9.6% reduction, P value: 0.17) concomitant with a minor but significant effect on nuclear signal (20.1% reduction, P value: 0.002; Fig. 2 B). In comparison, pretreatment with RNase T1 led to a significantly larger decrease in both nuclear and cytoplasmic S9.6 staining (Fig. 2 A), reducing total cellular S9.6 staining by 58.9% (P value: 9.4e-12; Fig. 2 B). Notably, RNase T1 treatment reduced average nuclear IF signal by 62.7% (P value: 8.9e-15) and led to a loss of nucleolar staining (Fig. 2, A and B). These effects were consistent across biological replicates and also observed in HeLa cells (Fig. S2, A and B). Since it was previously reported that S9.6 labeling of cells may be limited by formaldehyde fixation (Skourti-Stathaki et al., 2014), we also imaged formaldehyde-fixed U2OS cells. Application of S9.6 IF and RNase T1 and III pretreatments to formaldehyde-fixed cells largely recapitulated findings using methanol-fixed cells, indicating that formaldehyde fixation does not significantly alter the nature of S9.6 staining (Fig. S2, C and D).

We note that residual S9.6 signal was consistently observed after combined RNase T1 and RNase III treatment (Fig. S2 E). This signal could correspond to RNase T1– and RNase III–resistant RNAs owing to inherent limitations in the enzymes' abilities to fully degrade all RNA species, or accessibility to these RNAs in the context of fixed cells. We note that RNase T1 is an endonuclease that specifically cleaves ssRNA at guanine residues, and that RNase III efficiently fragments dsRNA rather than hydrolyzing it completely (Fig. S1 A). Regardless, addition of RNase H to the combined RNase T1/RNase III treatment did not further reduce S9.6 signal (Fig. S2 E). This suggests that genuine RNA:DNA hybrid signal could not be identified cytologically in normally cultured human cells even after removal of cellular RNAs by RNase T1 and RNase III. Taken together, these

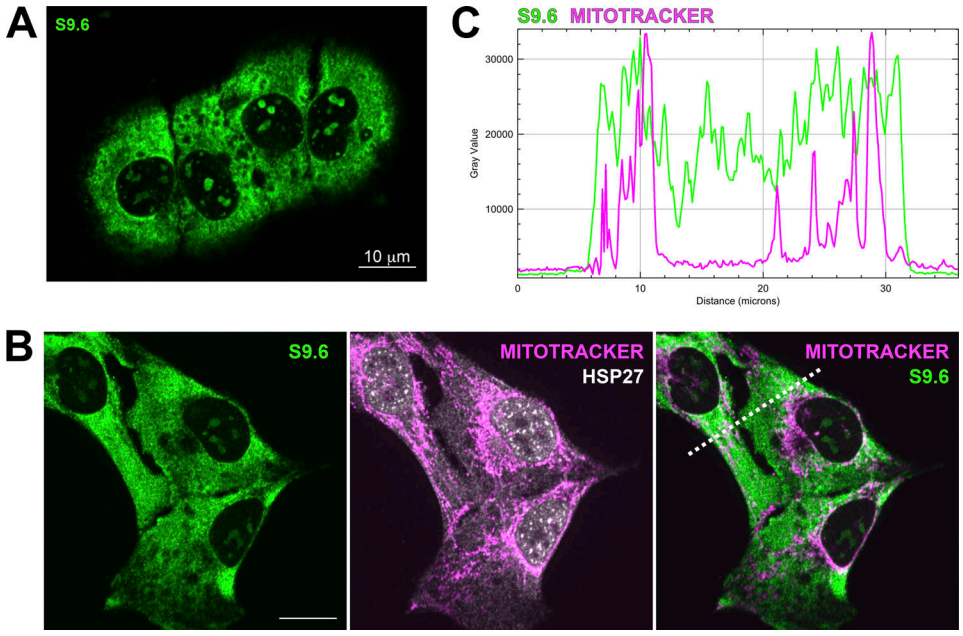

Figure 1. **Comparison of the cytological distributions of mitochondria and S9.6 signal in human cells. (A)** A single plane confocal IF image of methanol-fixed U2OS cells stained with S9.6 (green). **(B)** Maximum intensity projection of U2OS cells labeled with MitoTracker Deep Red FM (magenta) and stained with S9.6 (green) and anti-HSP27 (white). **(C)** Line scan plotting the intensity values for S9.6 and MitoTracker Deep Red FM in cells from the maximum intensity projection in B. Scale bar of 10 µm is indicated in A and B.

observations support that the majority of S9.6 signal in methanol-fixed and formaldehyde-fixed cells, in both the nucleus and the cytoplasm, stems from the binding of S9.6 to RNA, not RNA:DNA hybrids.

The S9.6 antibody can detect transfected RNA:DNA hybrids that are degraded by treatment with exogenous RNase H1 in situ

Given the negative results obtained above when testing for the RNA:DNA hybrid dependence of S9.6 IF signal, we sought a positive control for detection of RNA:DNA hybrids by S9.6 and degradation of RNA:DNA hybrids by RNase H1 in situ. Using 54-bp RNA:DNA hybrids that were fluorescently labeled with a 5′-Cy5 modification on the DNA strand, we transfected U2OS cells before fixation and again subjected samples to mock or RNase H1 treatments after fixation and before immunolabeling (Fig. 3 A). After lipofection with Cy5-labeled RNA:DNA hybrids, Cy5 foci were observed in and/or on the cell body of fixed cells (Fig. 3 B). Consistent with prior results (Rigby et al., 2014), Cy5 foci regularly appeared to be in endosomal-like compartments that excluded HSP27 (Fig. 3 B, inset), suggesting transfected hybrids had been internalized. Staining with S9.6 revealed prominent S9.6 foci that overlapped Cy5 foci (Fig. 3, B and C). As expected, there was also pancytoplasmic and nucleolar S9.6 IF signal that was independent of the focal Cy5 signal (Fig. 3, B and C). Transfection with unhybridized, single-stranded Cy5-labeled DNA oligos produced Cy5 foci with no accompanying S9.6 foci (Fig. S2 F), further supporting that the S9.6 foci arising from transfection with hybridized oligos were RNA:DNA hybrid dependent. These observations support that exogenous hybrids can be used in situ as a positive control for S9.6 immunolabeling.

To verify that exogenous RNase H1 treatment could effectively degrade hybrids in situ after methanol fixation, we compared the overlapping S9.6 intensities of individual Cy5 foci in transfected cells that were mock- and RNase H1–treated (Fig. 3, C and D). RNase H1 treatment reduced the average Cy5 focus–associated S9.6 signal by 69.7% (P value: 4e-26; Fig. 3 D), while the Cy5-independent cytoplasmic and nuclear signal persisted. This observation demonstrates that RNase H1 is active under these conditions and capable of efficiently degrading RNA:DNA hybrids in situ. Additionally, Cy5-associated S9.6 foci persisted after treatment with a combination of RNases T1 and III, while the Cy5-independent cytoplasmic and nuclear signal was qualitatively reduced (Fig. S2 F), further supporting that RNases T1 and III selectively degrade RNA that is detected by S9.6. Altogether, these results confirm that S9.6 can detect bona fide RNA:DNA hybrids in fixed cellular environments and that RNase H1 can degrade these substrates after fixation. This indicates that the S9.6 IF signal observed using normally cultured human cells is resistant to RNase H1 treatments not because of insufficiencies in RNase H1 treatment but because S9.6 is predominantly labeling RNase T1– and RNase III–sensitive RNA species.

RNA species detected in situ by S9.6 correspond primarily to rRNAs

We next sought to identify the cellular RNA species that are recognized by S9.6 in situ. We first hypothesized that these could correspond to structured pre-mRNAs and/or mRNA molecules. To test this hypothesis, we treated cells with the splicing inhibitor Pladienolide B (PladB) to trigger the formation of pre-mRNA–rich nuclear splicing speckles (Kotake et al., 2007). As expected, HeLa cells treated with PladB for 4 h showed

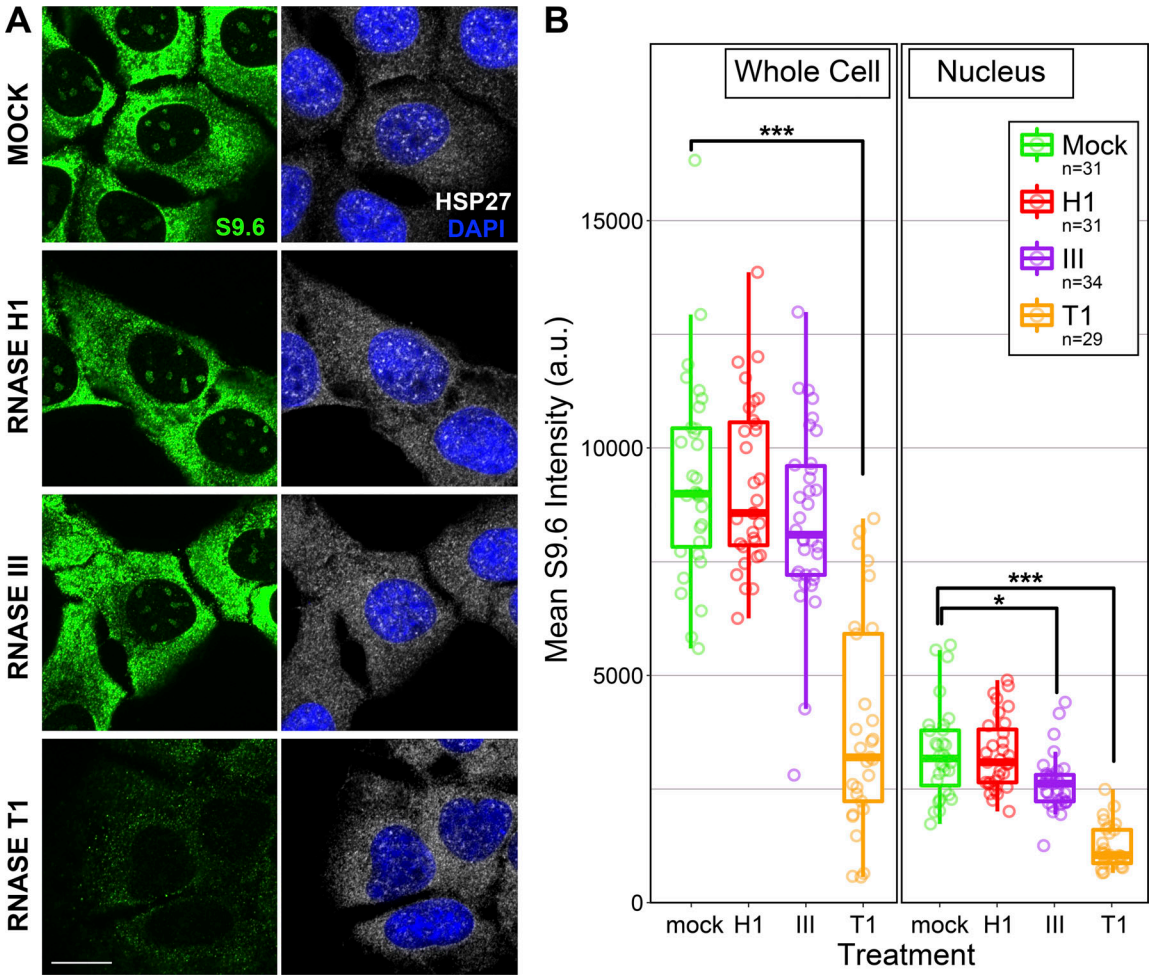

Figure 2. **Application of RNA- and RNA:DNA hybrid–specific nuclease pretreatments in S9.6 IF. (A)** Representative images of single planes of U2OS cells that were mock-treated or pretreated with RNase H1, RNase III, and RNase T1 for 1 h at room temperature before S9.6 staining. Scale bar, 10 µm. **(B)** Quantification of whole-cell and nuclear mean S9.6 intensities for individual cells that were mock- or enzyme-treated. Boxplots represent combined data from two biological replicates (*n* indicates the number of cells quantified), and P values were determined by a Wilcoxon Mann–Whitney test. *, P < 0.005; ***, P < 1e.10-10.

prominent nuclear speckles, visualized through the U2 spliceosome component SF3B4 (Fig. 4 A). Costaining of PladB-treated cells with S9.6 showed that these nuclear speckles were not labeled by S9.6 despite being an RNA-rich environment, while nucleoli remained prominent S9.6 targets. Given this observation, we next hypothesized that S9.6 may recognize rRNAs, which are abundantly produced in nucleoli and broadly localized throughout the cytoplasm. To test this, we used the Y10b antibody, which was raised against the 5.8S rRNA, a component of the 60S ribosome, to compare the distribution of rRNA and S9.6 staining. Consistent with prior observations (Gallouzi et al., 2000; Zhu et al., 2008), Y10b showed widespread cytoplasmic distribution accompanied by prominent nucleolar and faint nuclear signals (Fig. 4 B, left), recapitulating the cellular localization of S9.6. This overlap in staining patterns is unlikely to be due to inappropriate binding of RNA:DNA hybrids by Y10b, as evidenced by oligonucleotide gel shift assays showing little to no binding of RNA:DNA hybrids under conditions where S9.6 fully saturated the same substrate (Fig. S3 A). Costaining with mouse Y10b and an engineered rabbit S9.6 revealed a high degree of colocalization that was indistinguishable from that observed between mouse and rabbit S9.6 (Figs. 4 B and S3 B). Lastly, pretreatment of methanol-fixed cells with RNase T1, RNase III, and RNase H1 further confirmed that Y10b signal was highly RNase T1 sensitive, as expected, and insensitive to RNase III and RNase H1, mirroring the observations made with S9.6 (Figs. 4 C and S3 C).

To biochemically determine if S9.6 binds to rRNAs in the context of assembled ribosomal particles, we used highly purified human 40S and 60S ribosomal complexes (a kind gift from Dr. Christopher Fraser, University of California, Davis, Davis, CA) in native gel shift assays at 100 nM concentrations. S9.6 shifted both 40S and 60S complexes at 1:1 molar stoichiometries (Fig. 4 D), suggesting an affinity for native ribosomes in the nanomolar range. Furthermore, ribosomal subunits displayed increasing shifts in mobility with increasing S9.6 concentrations, indicating that S9.6 possesses multiple epitopes on each ribosome subunit (Fig. 4 D). By contrast, Y10b showed little to no binding to 40S complexes, as expected, and shifted 60S complexes, but to a lesser extent than S9.6 even under saturating concentrations. This indicates that, unlike S9.6, Y10b possesses fewer accessible binding sites on the 60S particles, likely leading to less pronounced gel shifts. Overall, these in vitro experiments,

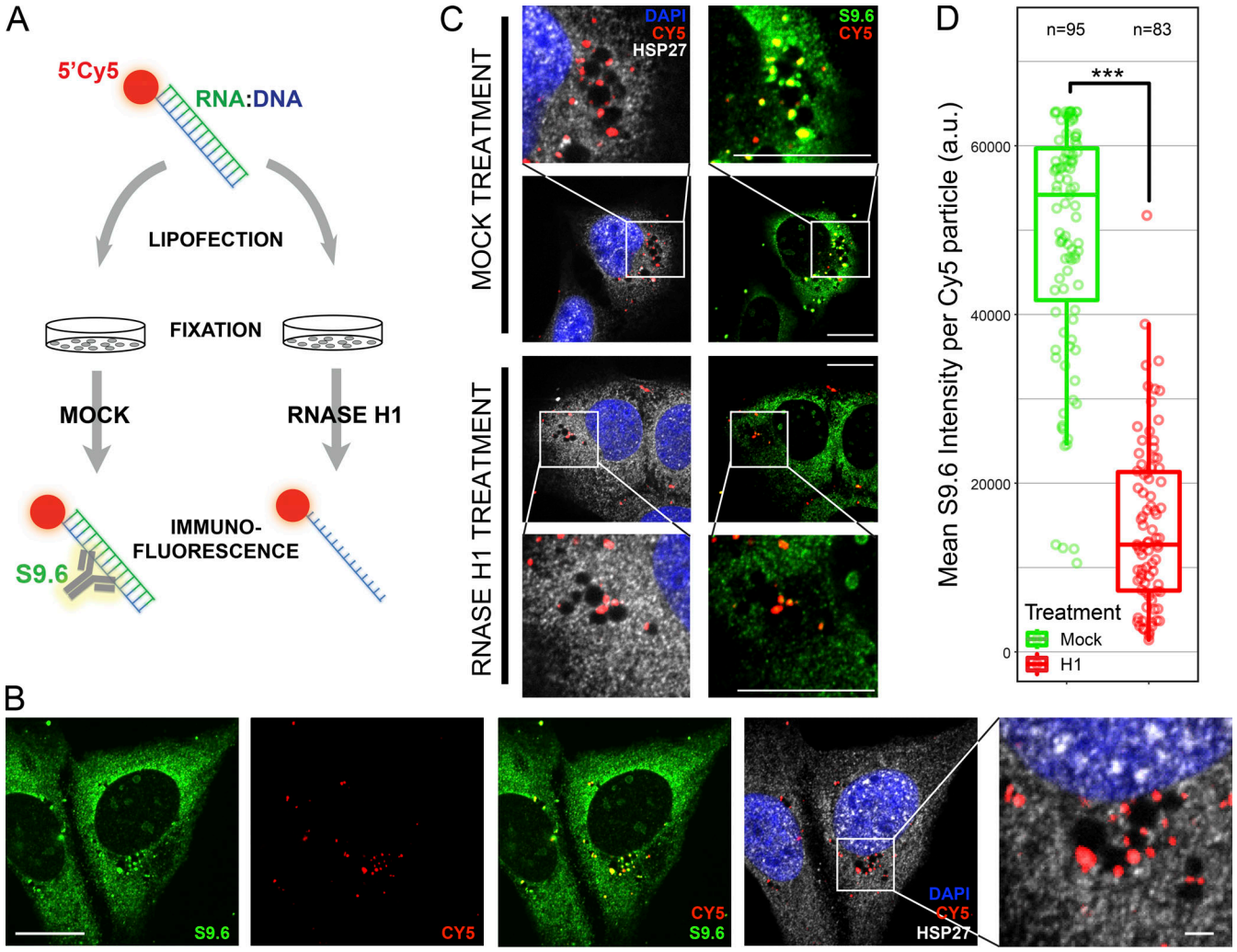

Figure 3. **Assessment of the RNA:DNA hybrid dependence and RNase H sensitivity of S9.6 IF using synthetic RNA:DNA hybrid transfections. (A)** Schematic of the RNA:DNA hybrid transfection strategy used as a positive control for in situ S9.6 staining and RNase H1 enzymatic activity. **(B)** Representative single plane image showing transfected U2OS cells containing Cy5-labeled RNA:DNA hybrids (red) that colocalize with S9.6 (green). Scale bars representing 10 µm and 1 µm (magnified inset, right) are indicated. **(C)** Representative single plane images of mock- and RNase H1-treated transfected cells (scale bar, 10 µm). **(D)** Quantification of the mean S9.6 intensities of individual Cy5 foci in mock- and RNase H1-treated cells. Plots represent combined data from two biological replicates (*n* indicates the number of particles measured), and P values were determined by a Wilcoxon Mann–Whitney test. ***, P < 1.10-15.

along with observations made in situ, establish that S9.6 can directly and preferentially recognize rRNAs.

Sonication DNA:RNA immunoprecipitation (DRIP) sequencing (sDRIP-seq) permits high-resolution, strand-specific R-loop mapping without interference from potential RNA contamination

The affinity of S9.6 for cellular RNAs has the potential to compromise the results of approaches other than IF microscopy. We previously showed that DRIP-based methods for which sequencing libraries are built from RNA, such as DRIP followed by cDNA sequencing (Sanz et al., 2016) or RNA:DNA immunoprecipitation followed by cDNA sequencing (Nojima et al., 2018), can suffer from significant caveats due to RNA binding by S9.6 (Chédin et al., 2021; Hartono et al., 2018). To circumvent this problem, we developed a new DRIP-based methodology that enables high-resolution, strand-specific R-loop mapping but for which sequencing libraries are built from immunoprecipitated DNA material, significantly lessening concerns regarding RNA contamination. The technique relies on an initial sonication step to fragment the genome, which permits higher-resolution mapping. Sonication also results in the breakage of the displaced single strand of R-loops, producing two-stranded RNA:DNA hybrids. Sequencing libraries are then built off the DNA strand of these hybrids in a stranded manner. To validate that sDRIP-seq maps are derived from genuine RNA:DNA hybrids, we subjected the sonicated materials to pretreatment with RNase H1. In parallel, we also performed RNase T1, RNase III, and combined RNase T1/III pretreatments to test the potential impacts of contaminating RNA. sDRIP-seq genome-wide maps obtained from human NTERA-2 cells showed predominantly genic, strand-specific signals associated with the direction of transcription (Fig. 5 A), consistent with prior R-loop mapping in this cell line (Sanz et al., 2016). Additionally, sDRIP-seq signal was nearly

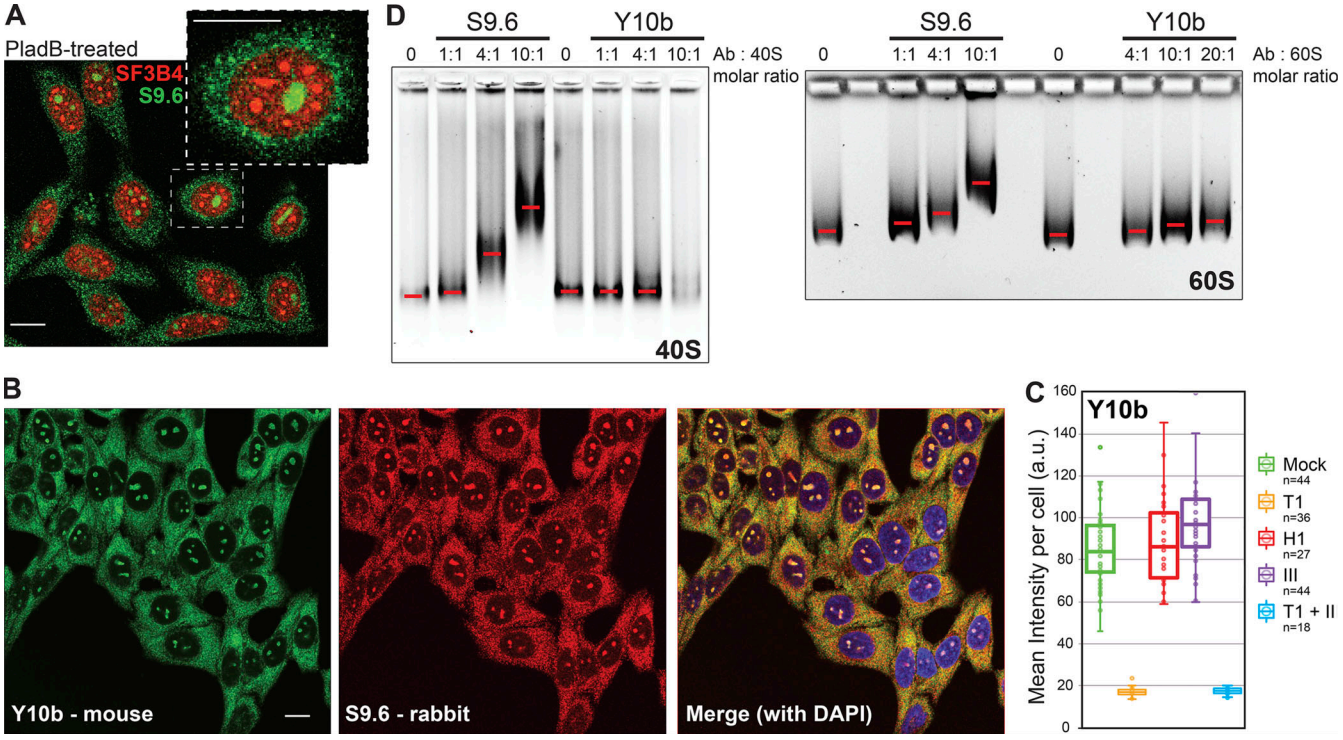

Figure 4. **Cytological evaluation and biochemical assay of ribosomal RNA binding by S9.6. (A)** Representative image of HeLa cells treated with 100 µM PladB for 4 h to induce the formation of splicing speckles. Splicing speckles were revealed using an antibody targeting SF3B4, a component of the U2 spliceosome (red). Cells were costained with S9.6 (green). The inset highlights a representative cell with clearly demarcated SF3B4 and S9.6 signals. **(B)** Representative image of HeLa cells stained with the anti-rRNA antibody Y10b (green, left panel). Cells were costained with an engineered rabbit S9.6 antibody (red, middle panel). A merged image with DAPI staining is shown at right. Scale bar, 10 µm for A and B. **(C)** Quantification of whole cell mean Y10b intensities for individual cells that were mock- or enzyme-treated. Boxplots represent combined data from two biological replicates (*n* indicates the number of cells quantified). **(D)** Native gel shift assays using purified human 40S (left) and 60S (right) ribosomes. Purified ribosomes (100 nM) were incubated for 10 min with increasing concentrations of S9.6 and Y10b, subjected to gel electrophoresis, and visualized with ethidium bromide staining. Red lines mark the approximated center of each band.

abrogated by RNase H1 treatment, supporting that sDRIP recovers genuine transcription-dependent RNA:DNA hybrids. Genome-wide correlation analysis showed that samples pretreated with RNase T1, RNase III, or a combination of the two enzymes were highly correlated (average correlations of ≥0.8) with the mock-treated control (Fig. 5 B). By contrast, RNase H1 treatment, and the associated loss of sDRIP signal, significantly reduced the average correlation (P value: 0.0009). These trends were further reflected in aggregate analyses of sDRIP signal over known R-loop hot spots such as transcription start sites, gene bodies, and transcription termination sites of human genes. These regions showed stereotypical enrichments and profiles that were not altered significantly by pretreatments with RNase T1 and/or RNase III but were lost with RNase H1 pretreatment (Fig. 5 C). In summary, sDRIP-seq permits strand-specific mapping of R-loops at high resolution in a manner that circumvents issues caused by the affinity of S9.6 for cellular RNAs.

In conclusion, we find that images obtained through IF microscopy using the S9.6 antibody predominantly reflect cellular RNA content in normally cultured human cells, not RNA:DNA hybrids. These findings are consistent with evidence that the S9.6 antibody has significant affinity for dsRNA (Hartono et al., 2018; Phillips et al., 2013) and therefore is not strictly RNA:DNA hybrid specific. However, our data suggest that the affinity of S9.6 for RNA does not apply uniformly across all RNA species. Unlike nucleoli, nuclear splicing speckles enriched for pre-mRNAs are not appreciably labeled by S9.6. Instead, we observe that S9.6 has a strong affinity for rRNAs and produces predominantly cytoplasmic and nucleolar IF signals highly concordant with the anti-rRNA antibody Y10b. While this work used normally cultured, unperturbed human cells, an array of gene perturbations and drug treatments have been reported to cause altered R-loop or RNA:DNA hybrid metabolism at least in part on the basis of changes in S9.6 IF staining patterns or intensity (Abakir et al., 2020; Bhatia et al., 2014; De Magis et al., 2019; Hodroj et al., 2017; Marinello et al., 2013; Mersaoui et al., 2019; Nguyen et al., 2018; Nguyen et al., 2017; Sollier et al., 2014). Many of the genes that have been ascribed roles in R-loop regulation participate in diverse RNA metabolic processes like transcription, RNA splicing, RNA processing, and RNA export (Paulsen et al., 2009). Alterations in RNA metabolism have the potential to impact the overall levels or subcellular distribution of various RNA species, including rRNAs. Ribosome pools are subject to tight regulation in response to various cellular stresses, leading to rapid modulation of nucleolar transcription, rRNA processing, and rRNA modifications (Yang et al., 2018). Such responses, in turn, regulate nuclear RNA import/export pathways, cell cycle and DNA repair mechanisms, as well as

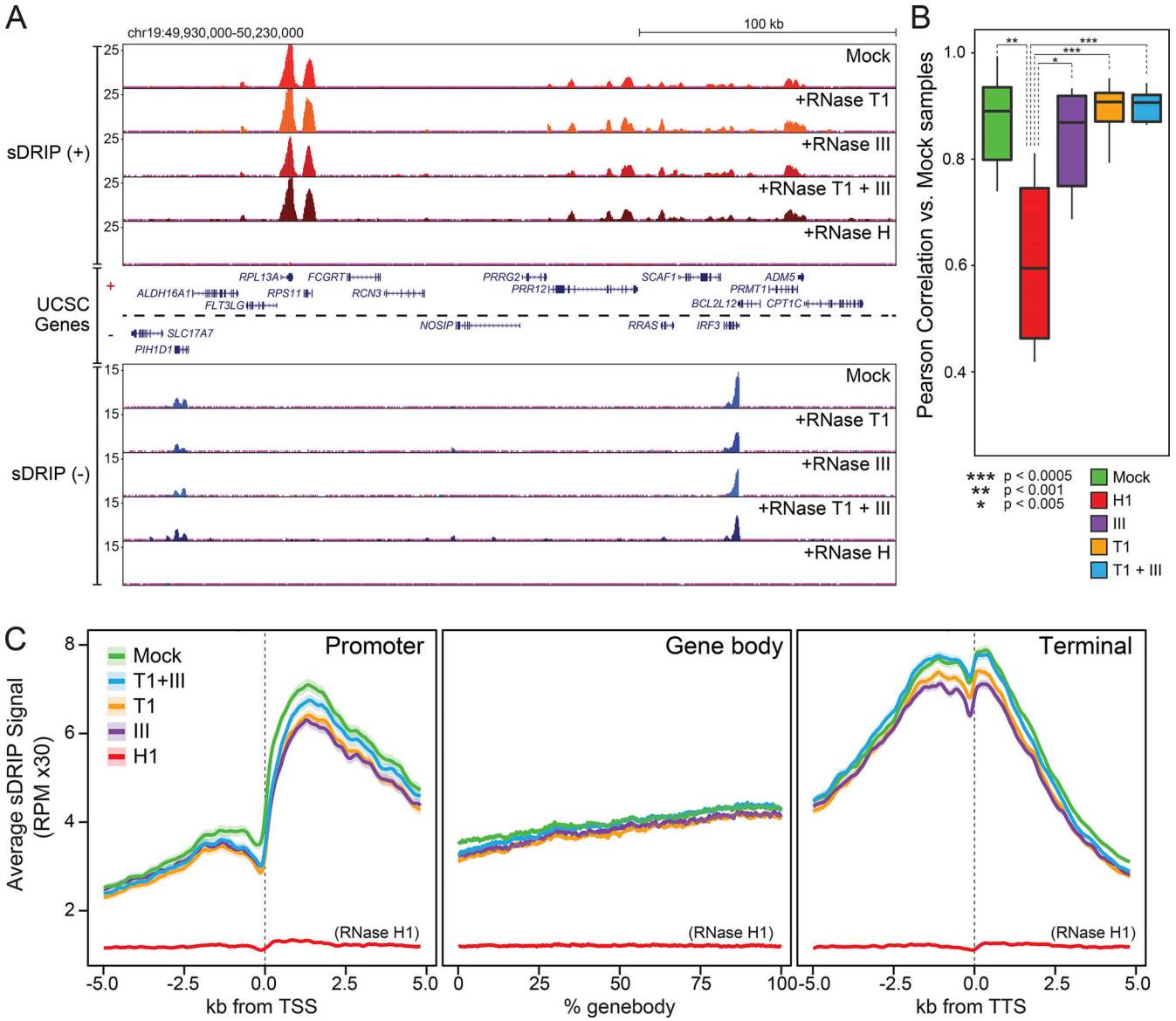

Figure 5. **Evaluation of the RNase sensitivity of sDRIP-seq. (A)** Genome browser tracks of a representative region of the human genome showing plus and minus strand sDRIP-seq signal obtained from mock-, RNase III–, RNase T1–, T1 and III–, and RNase H1–treated DRIP samples. **(B)** Boxplots showing the mean Pearson's correlations of sDRIP-seq signal between mock- and enzyme-treated samples. Correlation values were calculated from data from two replicates for each condition, and P values were determined by a Wilcoxon Mann–Whitney test. **(C)** Metaplots of sDRIP-seq signal over the transcription start site (TSS), gene body, and transcription termination site (TTS) of genes with RNA expression levels in the top 10% of expressed genes for mock- and enzyme-treated samples. For the TSS and TTS, the signal was plotted over a ±5-kb region. For gene bodies, the signal is shown as a percentile plot. Metaplots represent data from two replicates for each condition. Lines represent trimmed means, and accompanying shaded areas represent SEM.

growth rates (Lindström et al., 2018; Németh and Grummt, 2018). Any perturbation leading to nucleolar stress may therefore alter rRNA loads or distributions, which in turn could artifactually affect S9.6 staining due to the cross-reactivity of the antibody with rRNAs. We suggest that, where warranted, the controls outlined in this study should be used to validate previous observations made using S9.6 IF. It will be important to understand if and how various changes in R-loop abundance reported through S9.6 IF assays are influenced by changes in the production and distribution of rRNAs.

Lower cytoplasmic S9.6 staining and differences in the distribution of nuclear S9.6 signal have been reported by some studies (De Magis et al., 2019; Nguyen et al., 2018; Nguyen et al., 2017; Ross et al., 2020), differing from the observations made here. These differences can potentially be attributed to the use of various pre-extractions and washing steps before immunolabeling that may reduce the amounts of cellular RNAs. We chose not to employ these strategies, opting to comprehensively characterize the in situ reactivity of S9.6 in a manner unbiased by the introduction of these additional variables. Regardless of differences in sample preparation, the off-target binding of RNA, particularly rRNA, appears to be an inherent biochemical property of the S9.6 antibody that must be specifically controlled for. We recommend using exogenous RNase H treatments, along

with synthetic RNA:DNA hybrid transfections and RNA-specific nucleases, to verify both the efficacy of RNase H treatment and the specificity of S9.6 in situ. Additionally, imaging approaches may not be the only assays vulnerable to the affinity of S9.6 for RNA. We verified here that the mapping of R-loops in human cells using sDRIP-seq is not significantly affected by off-target recognition of RNA by S9.6. When sequencing libraries are built from DNA, not RNA, such as in DRIP-seq (Ginno et al., 2012), sDRIP-seq (this study), or the highly related quantitative DRIP methodology (Crossley et al., 2020), the ability of RNA to contribute off-target signal is essentially eliminated. However, when sequencing libraries are built from RNA, significant caveats can exist (Chédin et al., 2021). We suggest that, when possible, sequencing strategies that query R-loops through the DNA moieties of RNA:DNA hybrids, rather than RNA, should be favored. The method described here, sDRIP-seq, is ideal and permits high-resolution, strand-specific R-loop mapping. In all cases, stringent controls to ensure the resulting maps are sensitive to RNase H should be included. Coimmunoprecipitations using S9.6 to assay RNA:DNA hybrid–protein interactions may also be susceptible to isolating RNA-mediated interactions. An S9.6-based proteomic screen aimed at immunopurifying RNA:DNA hybrid–associated proteins overwhelmingly identified RNA-binding proteins, including >100 factors involved in ribosome biogenesis, rRNA modification, and rRNA processing (Cristini et al., 2018). While further biochemical characterization may show that these candidates are capable of directly recognizing RNA:DNA hybrids and/or R-loops, these results are also congruent with off-target recognition of rRNA by S9.6.

Ultimately, to mitigate the ability of RNA to interfere with S9.6-based approaches, degradation of cellular RNAs is critical. Using a standard enzyme like RNase A is an intuitive solution. However, we find that the RNA:DNA hybrid–degrading activity of RNase A makes use of the enzyme a suboptimal and unreliable control. While the use of RNase III rather than RNase A is an ideal way to specifically degrade dsRNA, we find that RNase III alone does not degrade a large portion of the RNAs that S9.6 can recognize in the context of imaging. Thus, to specifically and maximally degrade RNA while preserving RNA:DNA hybrids, we recommend systematic use of RNase III and RNase T1 treatments, as RNase T1 appears to specifically degrade a large portion of cellular RNAs that RNase III cannot. These pretreatments, coupled with RNase H controls, should help investigators use S9.6 in a thoroughly controlled manner that can account for the capacity of S9.6 to recognize RNA. We hope that the observations and controls established in this study can help ensure robust and accurate insights into RNA:DNA hybrid metabolism through informed use of the S9.6 antibody.

Materials and methods

Cell culture

U2OS and HeLa cells were obtained from American Type Culture Collection and grown in high-glucose DMEM supplemented with 10% FBS and 1% penicillin/streptomycin. Samples were seeded with cells at equal densities 1–2 d before experiments and were grown to ∼40–60% confluence. Cells were regularly tested and verified to be negative for mycoplasma before experiments.

Fixation and labeling for IF

All cell culture samples were grown, fixed, permeabilized, washed, enzymatically treated, immunostained, and imaged in 35-mm glass-bottom poly-D-lysine–coated dishes (P35GC-1.5-14-C; MatTek) using 2-ml volumes of medium and buffer solutions, unless indicated otherwise. All steps for fixation and IF were performed at room temperature, unless indicated otherwise. For methanol fixation, cells were fixed with 2 ml of ice-cold, 100% methanol for 10 min at −20°C. Cells were then washed once with PBS before subsequent preparation steps for IF. Permeabilization steps were unnecessary and omitted for methanol-fixed samples. For formaldehyde fixation, cells were fixed in freshly prepared 1% formaldehyde in PBS for 10 min. Fixation solutions were quenched with the addition of 200 µl PBS with 1 M glycine. Formaldehyde-fixed samples were washed once with PBS and then incubated in permeabilization buffer (PBS with 0.1% Triton X-100) for 10 min. For both methanol- and formaldehyde-fixed samples, samples were then incubated in staining buffer (TBST with 0.1% BSA [A9647-50G; Sigma-Aldrich]) for 10 min with rocking. Enzymatic treatments were done in staining buffer supplemented with 3 mM magnesium chloride with 1:200 dilutions of RNase T1 (EN0541; Thermo Fisher Scientific), ShortCut RNase III (M0245S; New England Biolabs), and/or recombinantly purified human RNase H1 (Loomis et al., 2014) and incubated with rocking for 1 h. Samples were subsequently washed by incubating with staining buffer for 10 min with rocking. For primary immunolabeling, samples were incubated in staining buffer with 1:1,000 dilutions of mouse S9.6 (purified from the HB-8730 hybridoma cell line), rabbit anti-HSP27 (06-478; Millipore) for cell body labeling, and/or rabbit anti-SF3B4 (sc365570; Santa Cruz; 1:200 dilution) for labeling splicing speckles. When indicated, an engineered rabbit S9.6 antibody (Ab01137-23; Absolute Antibody) and/or the mouse anti 5.8S rRNA Y10b antibody (NB100-662; Novus Biologicals) was used for staining at 1:1,000 dilutions. In all cases, primary antibodies were incubated for a minimum of 1 h at room temperature or overnight at 4°C with rocking. Samples were then washed once with staining buffer and incubated with 1:2,000 dilutions of secondary anti-mouse Alexa Fluor 488 conjugate (A28175; Invitrogen) and/or anti-rabbit Alexa Fluor 594 conjugate (A11037; Life Technologies) in the same manner as for the primary antibody incubation, with samples kept concealed from light from this step onward. Samples were then incubated with a 2.5 µg/ml DAPI dilution in staining buffer for 1–2 min and washed in TBST for 10 min with rocking before being stored in PBS at 4°C until imaging. Samples were imaged in PBS. To label mitochondria, live cells were stained with 500 nM MitoTracker Deep Red FM (Thermo Fisher Scientific) in complete medium for 15 min at 37°C and then incubated in MitoTracker-free complete medium for 15 min before fixation. For each experiment, all samples were prepared, treated, and stained in parallel from one master enzyme, antibody, and/or dye dilution to ensure uniform treatment and staining efficiencies.

Oligonucleotide preparation and transfection

Oligos were synthesized and HPLC-purified by Integrated DNA Technologies. Lyophilized DNA and RNA oligos were resuspended in autoclaved nanopure water to make 100 µM stocks. To prepare substrates for enzymatic tests and transfections, DNA and/or RNA

oligos were annealed in TBST at 10 µM concentrations by heating to 95°C for 3 min and then cooling to room temperature. Transfections were performed using Lipofectamine 2000 (Thermo Fisher Scientific) at a 1:50 dilution in 200 µl of Opti-MEM (Gibco) with a 1:100 dilution of RNA:DNA hybrids. The lipofectamine/RNA:DNA hybrid mix was then added dropwise to cells in 2 ml complete medium. Transfections were performed for 3 h, and cells were washed once with warm complete medium and incubated for an additional 6 h before fixation. The following oligonucleotide sequence, along with its complement and cognate RNA sequences, was used to design all nucleic acid substrates used: 5′-AGCTATAGTGACTGACGTTATCATGATGCTAGAGTCTCGATCGATAGTGTAGCT-3′.

Imaging and image analysis

Fixed cell imaging was performed using the spinning-disk module of an inverted objective fluorescence microscope (Marianas spinning-disk confocal real-time 3D confocal total internal reflection microscope; Intelligent Imaging Innovations) with a 63× or 100× objective. Image acquisition was done using SlideBook software (3i). For each experiment, all conditions were imaged in parallel, with identical exposure times and laser settings. Images were analyzed and quantified using ImageJ/Fiji programs, and statistics and data visualization were done using RStudio. P values were determined by a Wilcoxon Mann–Whitney test with the R wilcox.test() function. Whole-cell and nuclear mean S9.6 intensities were determined from a single plane for individual images. Whole-cell and nuclear regions were defined by thresholding or manual tracing using HSP27 and DAPI, respectively. For quantification of Cy5-associated S9.6 mean intensities, the Cy5 channel of each analyzed single-plane image was manually thresholded to generate a binary image. Analyze particles was applied to convert binary Cy5 images into regions of interest used to quantify the S9.6 intensities of Cy5-occupied regions of an image. Each region of interest was defined as an individual Cy5 particle.

Enzyme validation and gel electrophoresis

Single- and double-stranded oligonucleotide substrates were diluted in TBST with 0.1% BSA and 3 mM magnesium chloride to 1 µM final concentrations. Previously mentioned enzymes and RNase A (EN0531; Thermo Fisher Scientific) were used at a 1:200 final dilution and incubated with indicated nucleic acid substrates for 1 h at room temperature. To test ShortCut RNase III under manganese-supplemented conditions, reactions were performed in 50 mM Tris-HCl, pH 7.5, 75 mM KCl, and 3 mM $MnCl_2$ with 0.1% BSA. After incubation, a one-tenth volume of 50% glycerol was added to each sample before gel electrophoresis through 10% polyacrylamide TBE gels run at 80 V for 45 min. Gels were poststained with ethidium bromide and washed in TBE before imaging.

Native gel shifts with purified human ribosomal complexes

Purified human 40S and 60S ribosomes were a kind gift of Dr. Christopher Fraser and purified essentially as described (Sokabe and Fraser, 2014). In brief, constant amounts of ribosomes (100 nM) were incubated with increasing amounts of S9.6 or Y10b antibodies in binding buffer (20 mM Hepes, pH 7.5, 75 mM KCl, 2.5 mM $MgCl_2$, 0.25 mM DTT, and 10% glycerol) for 10 min at 37°C. Samples were then loaded on 1% agarose gels prepared in 1× THEM buffer (66 mM Hepes, pH 7.5, 34 mM Tris-HCl, pH 7.5, 0.1 mM EDTA, pH 8, and 2.5 mM $MgCl_2$) and run at 4°C for 60–90 min at 100 V in 1× THEM buffer. Gels were poststained with ethidium bromide and imaged.

DRIP followed by DNA sequencing

DRIP was performed as previously described (Sanz and Chedin, 2019), with modifications. Briefly, nucleic acids gently extracted from unfixed NTERA-2 cells were sheared by sonication (12 cycles of 15 s on/90 s off at high power) with a Bioruptor (Diagenode). 4.4 µg of sheared nucleic acids were incubated with 10 µg of S9.6 antibody for immunoprecipitation overnight at 4°C. To build strand-specific sequencing libraries, immunoprecipitated nucleic acids were subjected to a second-strand DNA synthesis step in which dUTP was used instead of dTTP. After verifying the quality of immunoprecipitation using quantitative PCR at standard positive and negative loci (Sanz and Chedin, 2019), strand-specific libraries were constructed, and DNA was sequenced using the HiSeq4000 platform. For RNase treatments, 15 µg of sheared DNA was treated with RNase H1, RNase T1, and/or RNase III for 1 h at 37°C using a 1:100 dilution of the stock enzymes in treatment buffer (50 mM Tris-HCl, pH 7.5, 75 mM KCl, and 3 mM $MgCl_2$). DNA was then purified with phenol/chloroform and ethanol precipitated before being used in S9.6 immunoprecipitations.

Normalization, peak calling, and data analysis for DRIP

Reads were mapped to the human genome using Bowtie2 (Langmead and Salzberg, 2012); only concordantly mapped reads were considered in case of paired-end samples. Normalization was performed based on total uniquely mapped reads with background correction. The MACS algorithm was used to call peaks with default parameters except for –nomodel (Zhang et al., 2008). For comparison of DRIP signals across treatments, read distributions were counted across 10-kb bins of the human genome. Pearson correlations were then systematically performed between each sample, excluding self-correlations. P values were calculated using the Wilcoxon Mann-Whitney test with the R wilcox.test() function. For XY plots, the averaged DRIP signal was measured over 10-kb bins for each treatment group (RNase T1, RNase III, RNase T1+III, and RNase H; y axis) and compared with averaged DRIP signal observed in the mock-treated samples (x axis). Linear regression values were then calculated for each comparison using the R lm() function.

Online supplemental material

Fig. S1 shows biochemical assays of the activity and specificity of all nucleases used and tested in this study using synthetic nucleic acid substrates. Fig. S2 shows additional IF experiments, including experiments using HeLa cells and formaldehyde-fixed cells, testing the effects of nuclease pretreatments on S9.6 antibody staining. Fig. S3 shows biochemical assays of the RNA:DNA hybrid binding capacity of the S9.6 antibody compared to the anti-ribosomal antibody Y10b, and IF images using both antibodies.

Acknowledgments

We thank Drs. Frank McNally, Jodi Nunnari, and Samantha Lewis for guidance and resources for IF microscopy and helpful suggestions. We thank Daisy Castillo-Guzman for help with R data visualization and light microscopy imaging, and Drs. Christopher Fraser and Masaaki Sokabe (University of California, Davis, Davis, CA) for the kind gift of purified human 40S and 60S complexes and useful advice.

Work in the Chédin laboratory is funded by a grant from the National Institutes of Health (R01 GM120607). J.A. Smolka was funded in part through the National Institutes of Health T32 training program in Molecular and Cellular Biology (T32 GM007377).

The authors declare no competing financial interests.

Author contributions: J.A. Smolka: conceptualization, methodology, investigation, formal analysis, writing, review, and editing; L.A. Sanz: methodology, investigation (developed and performed sDRIP, library construction); S.R. Hartono: formal analysis (bioinformatic analysis of sDRIP high-throughput DNA sequencing data); F. Chédin: funding acquisition, investigation (PladB treatments, Y10b IF, and ribosome-binding assays), formal analysis, writing, review, and editing.

Submitted: 10 April 2020
Revised: 1 February 2021
Accepted: 10 March 2021

References

Abakir, A., T.C. Giles, A. Cristini, J.M. Foster, N. Dai, M. Starczak, A. Rubio-Roldan, M. Li, M. Eleftheriou, J. Crutchley, et al. 2020. N^6-methyladenosine regulates the stability of RNA:DNA hybrids in human cells. *Nat. Genet.* 52:48–55. https://doi.org/10.1038/s41588-019-0549-x

Aguilera, A., and T. García-Muse. 2012. R loops: from transcription byproducts to threats to genome stability. *Mol. Cell.* 46:115–124. https://doi.org/10.1016/j.molcel.2012.04.009

Barroso, S., E. Herrera-Moyano, S. Muñoz, M. García-Rubio, B. Gómez-González, and A. Aguilera. 2019. The DNA damage response acts as a safeguard against harmful DNA-RNA hybrids of different origins. *EMBO Rep.* 20:e47250. https://doi.org/10.15252/embr.201847250

Bayona-Feliu, A., A. Casas-Lamesa, O. Reina, J. Bernués, and F. Azorín. 2017. Linker histone H1 prevents R-loop accumulation and genome instability in heterochromatin. *Nat. Commun.* 8:283. https://doi.org/10.1038/s41467-017-00338-5

Bhatia, V., S.I. Barroso, M.L. García-Rubio, E. Tumini, E. Herrera-Moyano, and A. Aguilera. 2014. BRCA2 prevents R-loop accumulation and associates with TREX-2 mRNA export factor PCID2. *Nature.* 511:362–365. https://doi.org/10.1038/nature13374

Boguslawski, S.J., D.E. Smith, M.A. Michalak, K.E. Mickelson, C.O. Yehle, W.L. Patterson, and R.J. Carrico. 1986. Characterization of monoclonal antibody to DNA.RNA and its application to immunodetection of hybrids. *J. Immunol. Methods.* 89:123–130. https://doi.org/10.1016/0022-1759(86)90040-2

Chédin, F. 2016. Nascent Connections: R-Loops and Chromatin Patterning. *Trends Genet.* 32:828–838. https://doi.org/10.1016/j.tig.2016.10.002

Chédin, F., S.R. Hartono, L.A. Sanz, and V. Vanoosthuyse. 2021. Best practices for the visualization, mapping, and manipulation of R-loops. *EMBO J.* 40:e106394. https://doi.org/10.15252/embj.2020106394

Choi, J., S.Y. Hwang, and K. Ahn. 2018. Interplay between RNASEH2 and MOV10 controls LINE-1 retrotransposition. *Nucleic Acids Res.* 46:1912–1926. https://doi.org/10.1093/nar/gkx1312

Cristini, A., M. Groh, M.S. Kristiansen, and N. Gromak. 2018. RNA/DNA Hybrid Interactome Identifies DXH9 as a Molecular Player in Transcriptional Termination and R-Loop-Associated DNA Damage. *Cell Rep.* 23:1891–1905. https://doi.org/10.1016/j.celrep.2018.04.025

Crossley, M.P., M. Bocek, and K.A. Cimprich. 2019. R-Loops as Cellular Regulators and Genomic Threats. *Mol. Cell.* 73:398–411. https://doi.org/10.1016/j.molcel.2019.01.024

Crossley, M.P., M.J. Bocek, S. Hamperl, T. Swigut, and K.A. Cimprich. 2020. qDRIP: a method to quantitatively assess RNA-DNA hybrid formation genome-wide. *Nucleic Acids Res.* 48:e84. https://doi.org/10.1093/nar/gkaa500

De Magis, A., S.G. Manzo, M. Russo, J. Marinello, R. Morigi, O. Sordet, and G. Capranico. 2019. DNA damage and genome instability by G-quadruplex ligands are mediated by R loops in human cancer cells. *Proc. Natl. Acad. Sci. USA.* 116:816–825. https://doi.org/10.1073/pnas.1810409116

El Hage, A., S.L. French, A.L. Beyer, and D. Tollervey. 2010. Loss of Topoisomerase I leads to R-loop-mediated transcriptional blocks during ribosomal RNA synthesis. *Genes Dev.* 24:1546–1558. https://doi.org/10.1101/gad.573310

El Hage, A., S. Webb, A. Kerr, and D. Tollervey. 2014. Genome-wide distribution of RNA-DNA hybrids identifies RNase H targets in tRNA genes, retrotransposons and mitochondria. *PLoS Genet.* 10:e1004716. https://doi.org/10.1371/journal.pgen.1004716

Gallouzi, I.E., C.M. Brennan, M.G. Stenberg, M.S. Swanson, A. Eversole, N. Maizels, and J.A. Steitz. 2000. HuR binding to cytoplasmic mRNA is perturbed by heat shock. *Proc. Natl. Acad. Sci. USA.* 97:3073–3078. https://doi.org/10.1073/pnas.97.7.3073

Ginno, P.A., P.L. Lott, H.C. Christensen, I. Korf, and F. Chédin. 2012. R-loop formation is a distinctive characteristic of unmethylated human CpG island promoters. *Mol. Cell.* 45:814–825. https://doi.org/10.1016/j.molcel.2012.01.017

Hamperl, S., M.J. Bocek, J.C. Saldivar, T. Swigut, and K.A. Cimprich. 2017. Transcription-Replication Conflict Orientation Modulates R-Loop Levels and Activates Distinct DNA Damage Responses. *Cell.* 170:774–786.e19. https://doi.org/10.1016/j.cell.2017.07.043

Hartono, S.R., A. Malapert, P. Legros, P. Bernard, F. Chédin, and V. Vanoosthuyse. 2018. The Affinity of the S9.6 Antibody for Double-Stranded RNAs Impacts the Accurate Mapping of R-Loops in Fission Yeast. *J. Mol. Biol.* 430:272–284. https://doi.org/10.1016/j.jmb.2017.12.016

Hatchi, E., K. Skourti-Stathaki, S. Ventz, L. Pinello, A. Yen, K. Kamieniarz-Gdula, S. Dimitrov, S. Pathania, K.M. McKinney, M.L. Eaton, et al. 2015. BRCA1 recruitment to transcriptional pause sites is required for R-loop-driven DNA damage repair. *Mol. Cell.* 57:636–647. https://doi.org/10.1016/j.molcel.2015.01.011

Hodroj, D., B. Recolin, K. Serhal, S. Martinez, N. Tsanov, R. Abou Merhi, and D. Maiorano. 2017. An ATR-dependent function for the Ddx19 RNA helicase in nuclear R-loop metabolism. *EMBO J.* 36:1182–1198. https://doi.org/10.15252/embj.201695131

Holt, I.J. 2019. The mitochondrial R-loop. *Nucleic Acids Res.* 47:5480–5489. https://doi.org/10.1093/nar/gkz277

Huertas, P., and A. Aguilera. 2003. Cotranscriptionally formed DNA:RNA hybrids mediate transcription elongation impairment and transcription-associated recombination. *Mol. Cell.* 12:711–721. https://doi.org/10.1016/j.molcel.2003.08.010

Hyjek, M., M. Figiel, and M. Nowotny. 2019. RNases H: Structure and mechanism. *DNA Repair (Amst.).* 84:102672. https://doi.org/10.1016/j.dnarep.2019.102672

Kabeche, L., H.D. Nguyen, R. Buisson, and L. Zou. 2018. A mitosis-specific and R loop-driven ATR pathway promotes faithful chromosome segregation. *Science.* 359:108–114. https://doi.org/10.1126/science.aan6490

Kinney, J.S., R.P. Viscidi, S.L. Vonderfecht, J.J. Eiden, and R.H. Yolken. 1989. Monoclonal antibody assay for detection of double-stranded RNA and application for detection of group A and non-group A rotaviruses. *J. Clin. Microbiol.* 27:6–12. https://doi.org/10.1128/JCM.27.1.6-12.1989

Koo, C.X., K. Kobiyama, Y.J. Shen, N. LeBert, S. Ahmad, M. Khatoo, T. Aoshi, S. Gasser, and K.J. Ishii. 2015. RNA polymerase III regulates cytosolic RNA:DNA hybrids and intracellular microRNA expression. *J. Biol. Chem.* 290:7463–7473. https://doi.org/10.1074/jbc.M115.636365

Kotake, Y., K. Sagane, T. Owa, Y. Mimori-Kiyosue, H. Shimizu, M. Uesugi, Y. Ishihama, M. Iwata, and Y. Mizui. 2007. Splicing factor SF3b as a target of the antitumor natural product pladienolide. *Nat. Chem. Biol.* 3:570–575. https://doi.org/10.1038/nchembio.2007.16

Langmead, B., and S.L. Salzberg. 2012. Fast gapped-read alignment with Bowtie 2. *Nat. Methods.* 9:357–359. https://doi.org/10.1038/nmeth.1923

Li, X., and J.L. Manley. 2005. Inactivation of the SR protein splicing factor ASF/SF2 results in genomic instability. *Cell.* 122:365–378. https://doi.org/10.1016/j.cell.2005.06.008

Lindström, M.S., D. Jurada, S. Bursac, I. Orsolic, J. Bartek, and S. Volarevic. 2018. Nucleolus as an emerging hub in maintenance of genome stability and cancer pathogenesis. *Oncogene.* 37:2351–2366. https://doi.org/10.1038/s41388-017-0121-z

Loomis, E.W., L.A. Sanz, F. Chédin, and P.J. Hagerman. 2014. Transcription-associated R-loop formation across the human FMR1 CGG-repeat region. *PLoS Genet.* 10:e1004294. https://doi.org/10.1371/journal.pgen.1004294

Marinello, J., G. Chillemi, S. Bueno, S.G. Manzo, and G. Capranico. 2013. Antisense transcripts enhanced by camptothecin at divergent CpG-island promoters associated with bursts of topoisomerase I-DNA cleavage complex and R-loop formation. *Nucleic Acids Res.* 41: 10110–10123. https://doi.org/10.1093/nar/gkt778

Mersaoui, S.Y., Z. Yu, Y. Coulombe, M. Karam, F.F. Busatto, J.Y. Masson, and S. Richard. 2019. Arginine methylation of the DDX5 helicase RGG/RG motif by PRMT5 regulates resolution of RNA:DNA hybrids. *EMBO J.* 38: e100986. https://doi.org/10.15252/embj.2018100986

Németh, A., and I. Grummt. 2018. Dynamic regulation of nucleolar architecture. *Curr. Opin. Cell Biol.* 52:105–111. https://doi.org/10.1016/j.ceb.2018.02.013

Nguyen, H.D., W.Y. Leong, W. Li, P.N.G. Reddy, J.D. Sullivan, M.J. Walter, L. Zou, and T.A. Graubert. 2018. Spliceosome Mutations Induce R Loop-Associated Sensitivity to ATR Inhibition in Myelodysplastic Syndromes. *Cancer Res.* 78:5363–5374. https://doi.org/10.1158/0008-5472.CAN-17-3970

Nguyen, H.D., T. Yadav, S. Giri, B. Saez, T.A. Graubert, and L. Zou. 2017. Functions of Replication Protein A as a Sensor of R Loops and a Regulator of RNaseH1. *Mol. Cell.* 65:832–847.e4. https://doi.org/10.1016/j.molcel.2017.01.029

Nojima, T., M. Tellier, J. Foxwell, C. Ribeiro de Almeida, S.M. Tan-Wong, S. Dhir, G. Dujardin, A. Dhir, S. Murphy, and N.J. Proudfoot. 2018. Deregulated Expression of Mammalian lncRNA through Loss of SPT6 Induces R-Loop Formation, Replication Stress, and Cellular Senescence. *Mol. Cell.* 72:970–984.e7. https://doi.org/10.1016/j.molcel.2018.10.011

Paulsen, R.D., D.V. Soni, R. Wollman, A.T. Hahn, M.C. Yee, A. Guan, J.A. Hesley, S.C. Miller, E.F. Cromwell, D.E. Solow-Cordero, et al. 2009. A genome-wide siRNA screen reveals diverse cellular processes and pathways that mediate genome stability. *Mol. Cell.* 35:228–239. https://doi.org/10.1016/j.molcel.2009.06.021

Phillips, D.D., D.N. Garboczi, K. Singh, Z. Hu, S.H. Leppla, and C.E. Leysath. 2013. The sub-nanomolar binding of DNA-RNA hybrids by the single-chain Fv fragment of antibody S9.6. *J. Mol. Recognit.* 26:376–381. https://doi.org/10.1002/jmr.2284

Rigby, R.E., L.M. Webb, K.J. Mackenzie, Y. Li, A. Leitch, M.A. Reijns, R.J. Lundie, A. Revuelta, D.J. Davidson, S. Diebold, et al. 2014. RNA:DNA hybrids are a novel molecular pattern sensed by TLR9. *EMBO J.* 33: 542–558. https://doi.org/10.1002/embj.201386117

Ross, N.T., F. Lohmann, S. Carbonneau, A. Fazal, W.A. Weihofen, S. Gleim, M. Salcius, F. Sigoillot, M. Henault, S.H. Carl, et al. 2020. CPSF3-dependent pre-mRNA processing as a druggable node in AML and Ewing's sarcoma. *Nat. Chem. Biol.* 16:50–59. https://doi.org/10.1038/s41589-019-0424-1

Sanz, L.A., and F. Chédin. 2019. High-resolution, strand-specific R-loop mapping via S9.6-based DNA-RNA immunoprecipitation and high-throughput sequencing. *Nat. Protoc.* 14:1734–1755. https://doi.org/10.1038/s41596-019-0159-1

Sanz, L.A., S.R. Hartono, Y.W. Lim, S. Steyaert, A. Rajpurkar, P.A. Ginno, X. Xu, and F. Chédin. 2016. Prevalent, Dynamic, and Conserved R-Loop Structures Associate with Specific Epigenomic Signatures in Mammals. *Mol. Cell.* 63:167–178. https://doi.org/10.1016/j.molcel.2016.05.032

Shen, W., H. Sun, C.L. De Hoyos, J.K. Bailey, X.H. Liang, and S.T. Crooke. 2017. Dynamic nucleoplasmic and nucleolar localization of mammalian RNase H1 in response to RNAP I transcriptional R-loops. *Nucleic Acids Res.* 45:10672–10692. https://doi.org/10.1093/nar/gkx710

Silva, S., L.P. Camino, and A. Aguilera. 2018. Human mitochondrial degradosome prevents harmful mitochondrial R loops and mitochondrial genome instability. *Proc. Natl. Acad. Sci. USA.* 115:11024–11029. https://doi.org/10.1073/pnas.1807258115

Skourti-Stathaki, K., and N.J. Proudfoot. 2014. A double-edged sword: R loops as threats to genome integrity and powerful regulators of gene expression. *Genes Dev.* 28:1384–1396. https://doi.org/10.1101/gad.242990.114

Skourti-Stathaki, K., K. Kamieniarz-Gdula, and N.J. Proudfoot. 2014. R-loops induce repressive chromatin marks over mammalian gene terminators. *Nature.* 516:436–439. https://doi.org/10.1038/nature13787

Skourti-Stathaki, K., N.J. Proudfoot, and N. Gromak. 2011. Human senataxin resolves RNA/DNA hybrids formed at transcriptional pause sites to promote Xrn2-dependent termination. *Mol. Cell.* 42:794–805. https://doi.org/10.1016/j.molcel.2011.04.026

Sokabe, M., and C.S. Fraser. 2014. Human eukaryotic initiation factor 2 (eIF2)-GTP-Met-tRNAi ternary complex and eIF3 stabilize the 43 S preinitiation complex. *J. Biol. Chem.* 289:31827–31836. https://doi.org/10.1074/jbc.M114.602870

Sollier, J., C.T. Stork, M.L. García-Rubio, R.D. Paulsen, A. Aguilera, and K.A. Cimprich. 2014. Transcription-coupled nucleotide excision repair factors promote R-loop-induced genome instability. *Mol. Cell.* 56:777–785. https://doi.org/10.1016/j.molcel.2014.10.020

Sorrells, S., S. Nik, M.J. Casey, R.C. Cameron, H. Truong, C. Toruno, M. Gulfo, A. Lowe, C. Jette, R.A. Stewart, and T.V. Bowman. 2018. Spliceosomal components protect embryonic neurons from R-loop-mediated DNA damage and apoptosis. *Dis. Model. Mech.* 11:dmm031583. https://doi.org/10.1242/dmm.031583

Sridhara, S.C., S. Carvalho, A.R. Grosso, L.M. Gallego-Paez, M. Carmo-Fonseca, and S.F. de Almeida. 2017. Transcription Dynamics Prevent RNA-Mediated Genomic Instability through SRPK2-Dependent DDX23 Phosphorylation. *Cell Rep.* 18:334–343. https://doi.org/10.1016/j.celrep.2016.12.050

Stirling, P.C., Y.A. Chan, S.W. Minaker, M.J. Aristizabal, I. Barrett, P. Sipahimalani, M.S. Kobor, and P. Hieter. 2012. R-loop-mediated genome instability in mRNA cleavage and polyadenylation mutants. *Genes Dev.* 26:163–175. https://doi.org/10.1101/gad.179721.111

Vanoosthuyse, V. 2018. Strengths and Weaknesses of the Current Strategies to Map and Characterize R-Loops. *Noncoding RNA.* 4:9. https://doi.org/10.3390/ncrna4020009

Wahba, L., S.K. Gore, and D. Koshland. 2013. The homologous recombination machinery modulates the formation of RNA-DNA hybrids and associated chromosome instability. *eLife.* 2:e00505. https://doi.org/10.7554/eLife.00505

Wang, I.X., C. Grunseich, J. Fox, J. Burdick, Z. Zhu, N. Ravazian, M. Hafner, and V.G. Cheung. 2018. Human proteins that interact with RNA/DNA hybrids. *Genome Res.* 28:1405–1414. https://doi.org/10.1101/gr.237362.118

Xu, W., H. Xu, K. Li, Y. Fan, Y. Liu, X. Yang, and Q. Sun. 2017. The R-loop is a common chromatin feature of the Arabidopsis genome. *Nat. Plants.* 3: 704–714. https://doi.org/10.1038/s41477-017-0004-x

Yang, K., J. Yang, and J. Yi. 2018. Nucleolar Stress: hallmarks, sensing mechanism and diseases. *Cell Stress.* 2:125–140. https://doi.org/10.15698/cst2018.06.139

Zeller, P., J. Padeken, R. van Schendel, V. Kalck, M. Tijsterman, and S.M. Gasser. 2016. Histone H3K9 methylation is dispensable for Caenorhabditis elegans development but suppresses RNA:DNA hybrid-associated repeat instability. *Nat. Genet.* 48:1385–1395. https://doi.org/10.1038/ng.3672

Zhang, Y., T. Liu, C.A. Meyer, J. Eeckhoute, D.S. Johnson, B.E. Bernstein, C. Nusbaum, R.M. Myers, M. Brown, W. Li, and X.S. Liu. 2008. Model-based analysis of ChIP-Seq (MACS). *Genome Biol.* 9:R137. https://doi.org/10.1186/gb-2008-9-9-r137

Zhu, C.H., J. Kim, J.W. Shay, and W.E. Wright. 2008. SGNP: an essential Stress Granule/Nucleolar Protein potentially involved in 5.8s rRNA processing/transport. *PLoS One.* 3:e3716. https://doi.org/10.1371/journal.pone.0003716

Supplemental material

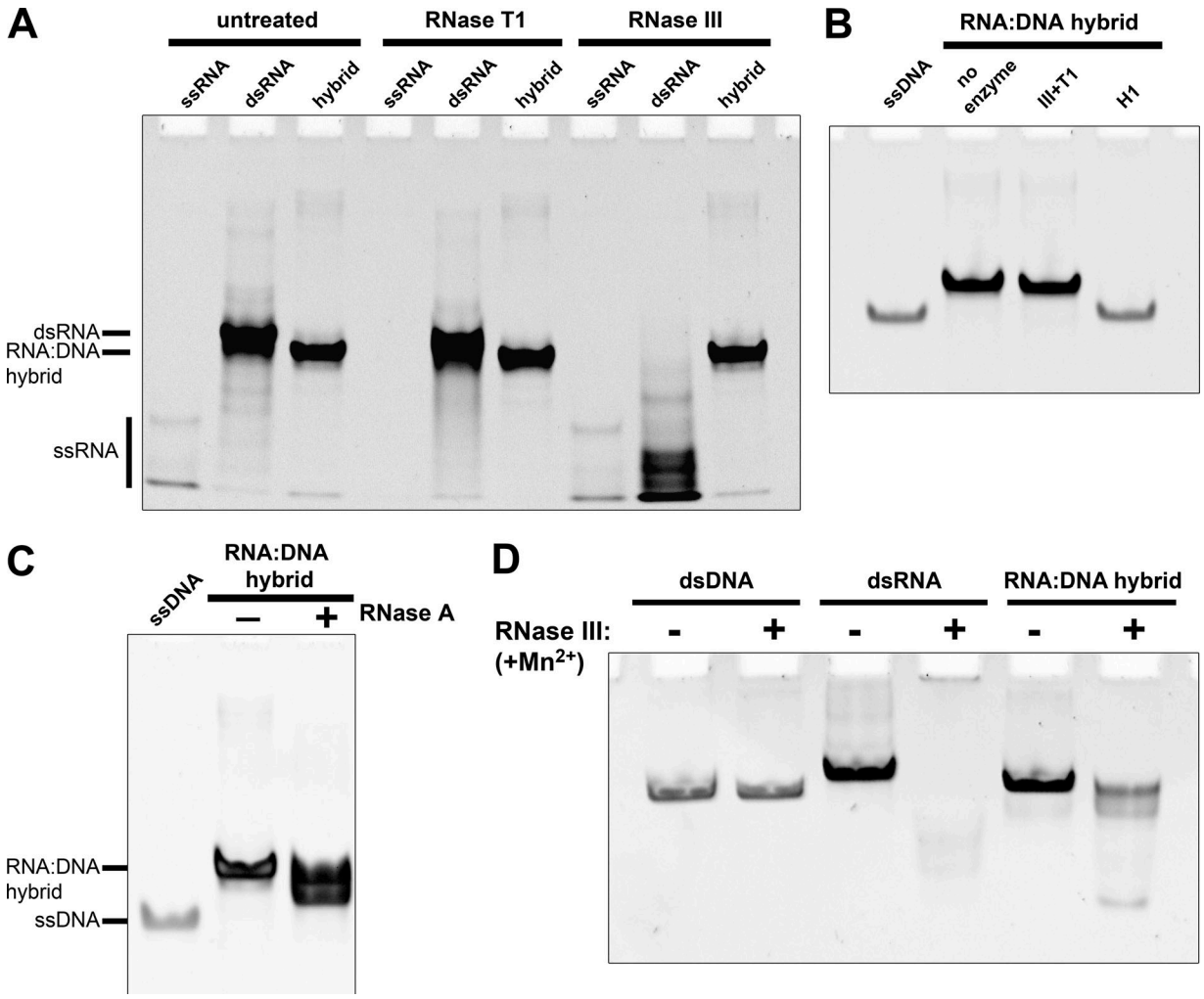

Figure S1. **Biochemical verification of the activities and specificities of RNases T1, III, H1, and A. (A)** Ethidium bromide–stained polyacrylamide gels showing 54 nucleotide ssRNA and 54-bp dsRNA and RNA:DNA hybrid substrates of the same sequence untreated and treated with RNase T1 and RNase III. Treatments were done for 1 h at room temperature. **(B)** RNA:DNA hybrids subjected to treatment with a combination of RNases T1 and III and treatment with RNase H1. **(C)** Treatment of RNA:DNA hybrid substrates with RNase A at 0.05 mg/ml. **(D)** Treatment of dsDNA, dsRNA, and RNA:DNA hybrids with ShortCut RNase III under manganese-supplemented conditions.

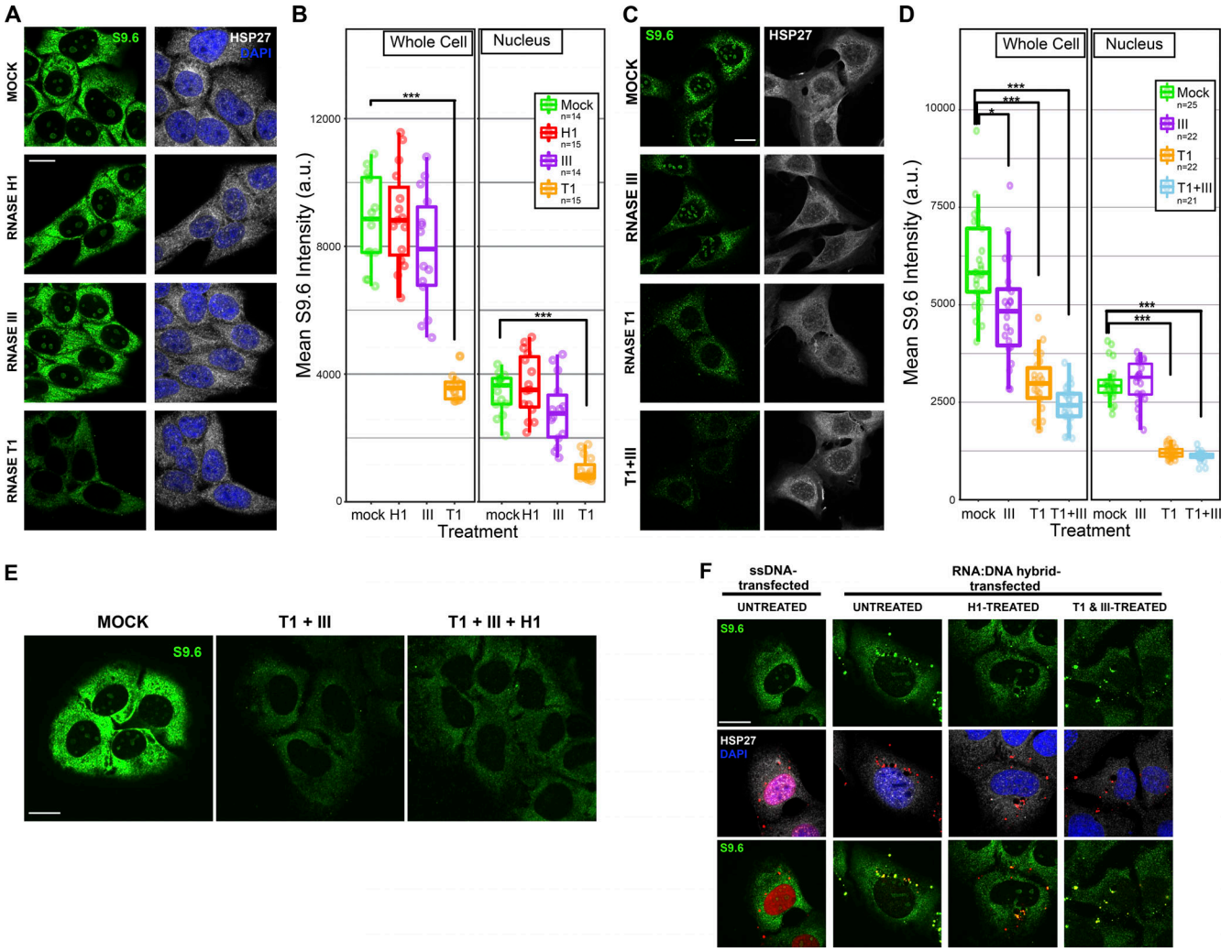

Figure S2. **Effects of individual and combined nuclease pretreatments on S9.6 IF in HeLa and formaldehyde-fixed U2OS cells.(A)** Representative images of single planes of HeLa cells that were mock-treated or pretreated with RNase H1, RNase III, and RNase T1 after fixation for 1 h at room temperature and stained with S9.6 (green), anti-HSP27 (white), and DAPI (blue). **(B)** Quantification of whole cell and nuclear mean S9.6 intensities for individual cells that were mock- or enzyme-treated. Boxplots represent combined data from two biological replicates (*n* indicates the number of cells quantified), and P values were determined by a Wilcoxon Mann–Whitney test (***, P < 1e-10). **(C)** Representative images of single planes of formaldehyde-fixed U2OS cells that were mock-treated or pretreated with RNase III, RNase T1, or a combination of both enzymes after fixation for 1 h at room temperature and stained with S9.6 (green) and anti-HSP27 (white). **(D)** Quantification of whole cell and nuclear mean S9.6 intensities for individual cells that were mock- or enzyme-treated. Boxplots represent combined data from two biological replicates (*n* indicates the number of cells quantified), and P values were determined by a Wilcoxon Mann–Whitney test (***, P < 1e-10; *, P < 0.01). **(E)** Images of single planes of methanol-fixed U2OS cells labeled with S9.6 that were mock-treated or pretreated with a combination of RNases T1 and III and a combination of RNases T1, III, and H1. **(F)** Images of single planes of U2OS cells transfected with 5′-Cy5–labeled ssDNA and RNA:DNA hybrids (red) and then fixed and immunolabeled with S9.6 (green) and anti-HSP27 (white). Note that Cy5 signal displayed more efficient nuclear accumulation with ssDNA than RNA:DNA hybrids. RNA:DNA hybrid-transfected cells were mock-treated and pretreated with RNase H1 and a combination of RNases T1 and III.

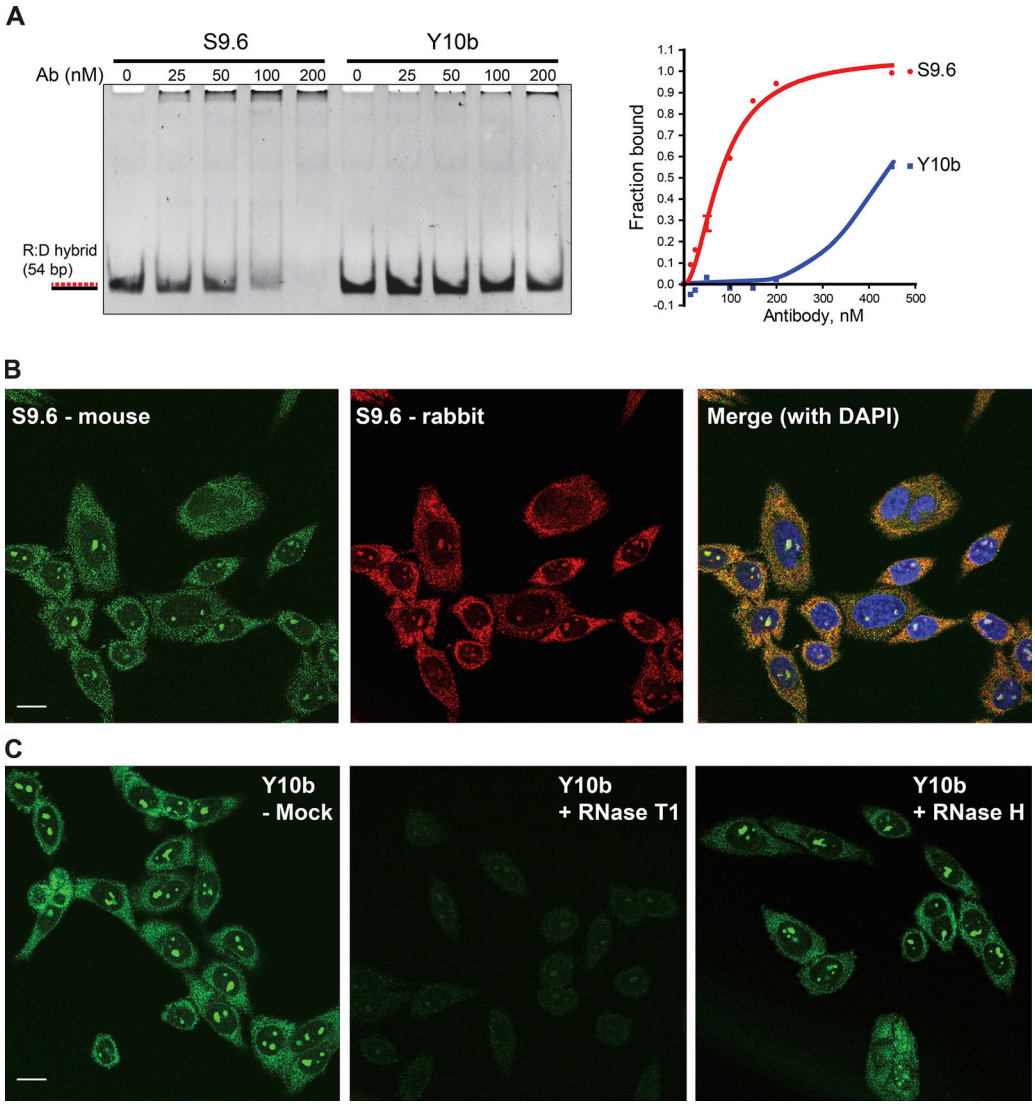

Figure S3. **Assessment of Y10b RNA:DNA hybrid and RNA binding in vitro and in situ. (A)** Left: 54-mer RNA:DNA hybrid oligonucleotide substrates (100 nM) were incubated with increasing concentrations of S9.6 and Y10b, and binding was evaluated after gel electrophoresis and ethidium bromide staining. Right: Quantification of gel shift assays comparing the affinity of Y10b for RNA:DNA hybrids to that of S9.6. **(B)** Representative images of methanol-fixed HeLa cells that were mock-treated or pretreated with RNase T1 and RNase H for 1 h at room temperature before staining with the Y10b antibody. **(C)** Representative images of methanol-fixed HeLa cells stained with mouse S9.6 (green) and an engineered rabbit S9.6 (red). Scale bar, 10 µm.